

Effects of isovector spin-orbit interaction on the charge-weak form factor difference in ^{48}Ca , ^{208}Pb , ^{90}Zr and ^{62}Ni

Tong-Gang Yue,^{1,2} Zhen Zhang,^{3,*} and Lie-Wen Chen^{1,†}

¹*State Key Laboratory of Dark Matter Physics, Key Laboratory for Particle Astrophysics and Cosmology (MOE), and Shanghai Key Laboratory for Particle Physics and Cosmology, School of Physics and Astronomy, Shanghai Jiao Tong University, Shanghai 200240, China*

²*Tsung-Dao Lee Institute, Shanghai Jiao Tong University, Shanghai 201210, China*

³*Sino-French Institute of Nuclear Engineering and Technology, Sun Yat-sen University, Zhuhai 519082, China*

(Dated: March 4, 2026)

The nucleon spin-orbit interaction is a cornerstone of modern nuclear theory, yet its isospin dependence remains elusive due to the lack of clean experimental probes. It has been recently demonstrated that within Skyrme-like energy density functionals, the charge-weak form factor difference ΔF_{CW} in ^{48}Ca exhibits remarkable sensitivity to the isovector spin-orbit (IVSO) interaction, and that a significantly enhanced IVSO strength can resolve the PREX-CREX puzzle. Extending this analysis to other nuclei, we identify that ^{90}Zr , with its ten spin-orbit unpaired $1g_{9/2}$ neutrons, displays a ΔF_{CW} sensitivity to the IVSO strength similar to that of ^{48}Ca , arising from modifications to the central mean-field potential rather than the one-body spin-orbit potential. In contrast, ^{208}Pb and ^{62}Ni remain largely insensitive to the IVSO interaction. Furthermore, this structure-driven distinction suggests a distinct experimental strategy: future parity-violating electron scattering measurements on ^{48}Ca and ^{90}Zr would enable a more precise determination of the IVSO strength, while measurements on ^{208}Pb and ^{62}Ni can serve as purer constraints on the symmetry energy slope.

I. INTRODUCTION

The spin-orbit (SO) interaction, emerging from the relativistic effect [1, 2], plays a crucial role across many branches of physics—from the elementary quark-gluon dynamics [3, 4] to macroscopic phenomena in condensed matter and optics [5, 6]. Historically, it was first introduced in atomic physics in the 1920s to explain the fine structure of atomic spectra [1, 7]. In 1949, Mayer [8] and Jensen [9] incorporated a strong nucleon SO interaction into the nuclear shell model, successfully explaining the emergence of magic numbers in nuclei. This achievement marked a milestone in nuclear theory, establishing SO interaction as a key mechanism for understanding nuclear structure, stability, and shell evolution.

Since nuclei are composed of protons and neutrons, a natural question then arises: is the SO interaction identical for protons and neutrons in the nuclei? Microscopically, the pronounced SO interaction in nuclei splits a single-particle energy level with the same orbital angular momentum l ($l \neq 0$) into two distinct sub-levels with different total angular momentum j . This SO splitting is the most readily observable manifestation of the underlying SO interaction. For nuclei close to the β -stability line, the isospin asymmetry (measuring difference between neutron and proton numbers) is small, leading to similar magnitudes of SO splitting for protons and neutrons. In contrast, the nuclei far from stability, particularly those with a large neutron excess, exhibit marked differences between proton and neutron

SO splittings [10]. This observation suggests the isospin-dependent nature of the SO interaction, i.e., an isovector spin-orbit (IVSO) interaction. However, since the single-nucleon energy levels cannot be directly measured and the impact of SO interaction has a complex interplay with, e.g., tensor force [11] and nucleon effective masses [12], the strength of the IVSO interaction is still largely uncertain, which poses a big challenge in modern nuclear theory [13].

Due to the lack of clean and sensitive experimental probes, the roles of the IVSO interaction have been longly overlooked, and its strength is traditionally considered to be much weaker than the isoscalar one. For instance, in conventional relativistic mean-field models with σ , ω and ρ mesons, the SO interaction naturally emerges from the Dirac equation and displays very weak isospin-dependence [14, 15]. However, it is expected that the inclusion of isovector-scalar δ meson and isovector Fock (exchange) terms in covariant nuclear energy density functionals (EDFs) should significantly enhance its isospin-dependence [16]. For conventional nonrelativistic Skyrme EDFs, the strength of IVSO interaction is only one third that of the isoscalar term [17]. Recent studies have demonstrated that the charge-weak form factor difference in ^{48}Ca , recently determined model-independently by the CREX experiment [18] at JLab, is sensitive to the IVSO interaction. Specifically, a strong IVSO interaction, about four times stronger than conventional parametrizations, can resolve the PREX-CREX puzzle (the phenomenon that theoretical models fail to simultaneously reproduce both experimental results within one sigma) [19–32]. The very recent study based on covariant density functionals, in point-coupling with isovector tensor coupling interactions, has already reached a conclusion consistent with nonrelativistic models [33].

* Corresponding author; zhangzh275@mail.sysu.edu.cn

† Corresponding author; lwchen@sjtu.edu.cn

In this work, through an analysis of the single-particle levels in ^{48}Ca and ^{208}Pb , we demonstrate that the conventional shell closures, including the magic numbers, are well reproduced and retain their robustness even in the presence of a strong isovector spin-orbit (IVSO) interaction. Extending this analysis, we identify a structural correspondence between ^{90}Zr and ^{48}Ca , as well as between ^{62}Ni and ^{208}Pb , based on their analogous spin-orbit saturation properties. This analogy implies that the charge-weak form factor difference $\Delta F_{\text{CW}} = F_C - F_W$, and thereby the neutron skin, exhibits significant sensitivity to the IVSO strength in ^{90}Zr , while remaining largely insensitive in ^{62}Ni . The broader implications of this nucleus-dependent sensitivity are discussed in what follows.

II. METHODS

A. Extended Skyrme EDF within Hartree-Fock-Bogoliubov (HFB) theory

In the present work, we use a nonrelativistic nuclear EDF based on the extended Skyrme interaction [34], with further incorporation of a zero-range tensor force [35]. The adopted extended Skyrme interaction v_{eSky} differs from conventional Skyrme interaction v_{Sky} by including momentum-dependent many-body force, that is

$$v_{\text{eSky}} = v_{\text{Sky}} + v', \quad (1)$$

where, the conventional Skyrme interaction v_{Sky} reads (see, e.g., Ref. [36]):

$$\begin{aligned} v_{\text{Sky}} = & t_0 (1 + x_0 P_\sigma) \delta(r) \\ & + \frac{1}{2} t_1 (1 + x_1 P_\sigma) [k'^2 \delta(r) + \delta(r) k^2] \\ & + t_2 (1 + x_2 P_\sigma) k' \cdot \delta(r) k + \frac{1}{6} t_3 (1 + x_3 P_\sigma) [\rho(R)]^\alpha \delta(r) \\ & + i W_0 (\sigma_1 + \sigma_2) \cdot [k' \times \delta(r) k], \end{aligned} \quad (2)$$

and

$$\begin{aligned} v' = & \frac{1}{2} t_4 (1 + x_4 P_\sigma) [k'^2 \rho(R)^\beta \delta(r) + \delta(r) \rho(R)^\beta k^2] \\ & + t_5 (1 + x_5 P_\sigma) k' \cdot \rho(R)^\gamma \delta(r) k. \end{aligned} \quad (3)$$

Here, $r = r_1 - r_2$, $R = \frac{1}{2}(r_1 + r_2)$, $k = \frac{1}{2i}(\nabla_1 - \nabla_2)$ is the relative momentum with k' being its conjugate acting on the left, the σ are Pauli spin operators, $P_\sigma = \frac{1}{2}(1 + \sigma_1 \cdot \sigma_2)$ is the spin exchange operator, and $\rho(R) = \rho_n(R) + \rho_p(R)$ is the total local density with ρ_n and ρ_p being neutron and proton densities, respectively. The $t_0 \sim t_5$, $x_0 \sim x_5$, α , β and γ are adjustable ‘‘Skyrme parameters’’, and W_0 is the SO interaction parameter. For simplicity, both β and γ are set to be unity as in Ref. [37].

For the tensor force, we use the following zero-range form [35]

$$\begin{aligned} V_T = & \frac{1}{2} T \left\{ \left[(\sigma_1 \cdot k') (\sigma_2 \cdot k') - \frac{1}{3} k'^2 (\sigma_1 \cdot \sigma_2) \right] \delta(r) \right. \\ & \left. + \delta(r) \left[(\sigma_1 \cdot k) (\sigma_2 \cdot k) - \frac{1}{3} k^2 (\sigma_1 \cdot \sigma_2) \right] \right\} \\ & + U \left\{ (\sigma_1 \cdot k') \delta(r) (\sigma_2 \cdot k) - \frac{1}{3} (\sigma_1 \cdot \sigma_2) [k' \cdot \delta(r) k] \right\}, \end{aligned} \quad (4)$$

where T and U quantify the magnitude of the tensor force in states of even and odd relative motion, respectively. In practical calculations, the parameters α_T and β_T are employed in place of U and T , where α_T and β_T are expressed as:

$$\alpha_T = \frac{5}{12} U, \quad \beta_T = \frac{5}{24} (T + U). \quad (5)$$

In addition, for calculations of open-shell nuclei, we take into account pairing force of the form

$$V_p(r, r') = V_0 \left[1 - \frac{\rho(r)}{2\rho_0} \right] \delta(r - r'), \quad (6)$$

where V_0 is the pairing strength and $\rho_0 = 0.16 \text{ fm}^{-3}$.

Based on above extended Skyrme interaction, tensor force and pairing force, we can obtain the EDF within the HFB theory. Under the assumption of time-reversal invariance, the energy of a nucleus can be written as the integral of a purely local EDF \mathcal{E} . For details on the HFB calculation based on Skyrme EDF, see e.g. Ref. [38]. In the following, we focus on potential density $\mathcal{E}_{\text{eSky}}$ for extended Skyrme interaction and tensor force, which can be expressed in terms of local density ρ_q , kinetic-energy density τ_q and spin-current density J_q of neutrons ($q = n$) and protons ($q = p$) defined by

$$\rho_q(r) = \sum_i v_i^2 |\varphi_i(r)|^2, \quad (7)$$

$$\tau_q(r) = \sum_i v_i^2 |\nabla \varphi_i(r)|^2, \quad (8)$$

$$J_q(r) = -i \sum_i v_i^2 \varphi_i^\dagger(r) \nabla \times \hat{\sigma} \varphi_i(r). \quad (9)$$

Here, φ_i is the wave function of canonical state i , v_i is corresponding occupation probability, and the sum runs over all states for the same given q . By further defining the isoscalar densities

$$\rho = \rho_n + \rho_p, \quad \tau = \tau_n + \tau_p, \quad J = J_n + J_p,$$

and isovector densities

$$\tilde{\rho} = \rho_n - \rho_p, \quad \tilde{\tau} = \tau_n - \tau_p, \quad \tilde{J} = J_n - J_p,$$

the $\mathcal{E}_{\text{eSky}}$ can be written as

$$\begin{aligned}
\mathcal{E}_{\text{eSky}} = & \frac{B_0 + B_3\rho^\alpha}{2}\rho^2 - \frac{B'_0 + B'_3\rho^\alpha}{2}\tilde{\rho}^2 \\
& + (B_1 + B_4\rho^\beta + B_5\rho^\gamma)\rho\tau \\
& - (B'_1 + B'_4\rho^\beta + B'_5\rho^\gamma)\tilde{\rho}\tilde{\tau} \\
& + \frac{2B_2 + (2\beta + 3)B_4\rho^\beta - B_5\rho^\gamma}{4}(\nabla\rho)^2 \\
& - \frac{2B'_2 + 3B'_4\rho^\beta - B'_5\rho^\gamma}{4}(\nabla\tilde{\rho})^2 \\
& - \frac{\beta B'_4}{2}\rho^{\beta-1}\tilde{\rho}\nabla\rho \cdot \nabla\tilde{\rho} \\
& + \frac{C_1 + C_2\rho^\beta + C_3\rho^\gamma}{2}J^2 + \frac{C'_1 + C'_2\rho^\beta + C'_3\rho^\gamma}{2}\tilde{J}^2 \\
& + \frac{b_{\text{IS}}}{2}\nabla\rho \cdot J + \frac{b_{\text{IV}}}{2}\nabla\tilde{\rho} \cdot \tilde{J} \\
& + \frac{\alpha_T + \beta_T}{4}J^2 + \frac{\alpha_T - \beta_T}{4}\tilde{J}^2. \tag{10}
\end{aligned}$$

The coefficients B_i , B'_i , C_i and C'_i are uniquely related to the Skyrme parameters t_i and x_i by

$$\begin{aligned}
B_0 &= 3t_0/4, \\
B'_0 &= t_0(1/2 + x_0)/2, \\
B_1 &= (3t_1 + 5t_2)/16 + t_2x_2/4, \\
B'_1 &= [t_1(1/2 + x_1) - t_2(1/2 + x_2)]/8, \\
B_2 &= (9t_1 - 5t_2)/32 - t_2x_2/8, \\
B'_2 &= [3t_1(1/2 + x_1) + t_2(1/2 + x_2)]/16, \\
B_3 &= t_3/8, \\
B'_3 &= t_3(1/2 + x_3)/12, \\
B_4 &= 3t_4/16, \\
B'_4 &= t_4(1/2 + x_4)/8, \\
B_5 &= (5t_5)/16 + t_5x_5/4, \\
B'_5 &= -t_5(1/2 + x_5)/8, \\
C_1 &= \eta_{\text{tIs}}[t_1(1/2 - x_1) - t_2(1/2 + x_2)]/8, \\
C'_1 &= \eta_{\text{tIs}}(t_1 - t_2)/16, \\
C_2 &= \eta_{\text{tIs}}t_4(1/2 - x_4)/8, \\
C'_2 &= \eta_{\text{tIs}}t_4/16, \\
C_3 &= -\eta_{\text{tIs}}t_5(1/2 + x_5)/8, \\
C'_3 &= -\eta_{\text{tIs}}t_5/16.
\end{aligned} \tag{11}$$

The b_{IS} and b_{IV} characterize the isoscalar and isovector spin-orbit strengths, respectively. In the conventional Skyrme formulation, these are related by $b_{\text{IS}} = 3b_{\text{IV}} = 3W_0/2$, where W_0 is the Skyrme spin-orbit parameter. In this work, following Ref. [15], we treat b_{IS} and b_{IV} as free and independent parameters to explore the role of the isovector spin-orbit interaction.

Following Ref. [19], we employ the eS53 and eS250 Skyrme EDFs constructed therein, which differ primarily in their IVSO strength: eS53 adopts the conventional relation $b_{\text{IV}} = b_{\text{IS}}/3$, while eS250 features a significantly enhanced $b_{\text{IV}} \approx 250 \text{ MeV}\cdot\text{fm}^5$ that simultaneously reproduces the CREX and PREX-II results.

The tensor-related J_q^2 terms in Eq. (11) involve the coefficients C_i and C'_i . These terms are often omitted in many Skyrme EDFs, and we use the parameter η_{tIs} as a switch factor [12] to control their inclusion, with $\eta_{\text{tIs}} = 1$ and 0 representing their full inclusion and absence, respectively. For the EDFs employed in this work, $\eta_{\text{tIs}} = 0$ for both eS53 and eS250, while $\eta_{\text{tIs}} = 1$ for the eS500_T, with an extremely strong IVSO interaction of $b_{\text{IV}} = 500 \text{ MeV}\cdot\text{fm}^5$ together with zero-range tensor force, are introduced in Ref. [19].

Based on the above EDF, nuclear ground-state properties are calculated by solving the HFB equations. The single nucleon Hamiltonian entering into the HFB equation can be expressed as

$$\hat{h}_q = -\nabla \cdot \frac{\hbar^2}{2m_q^*}\nabla + U_q + iW_q \cdot (\sigma \times \nabla), \quad q = n, p, \tag{12}$$

where the single-nucleon fields can be derived from the energy density \mathcal{E} by

$$\frac{\hbar^2}{2m_q^*} = \frac{\partial\mathcal{E}}{\partial\tau_q}, \quad U_q = \frac{\partial\mathcal{E}}{\partial\rho_q} - \nabla \cdot \frac{\partial\mathcal{E}}{\partial[\nabla\rho_q]}, \quad W_q = \frac{\partial\mathcal{E}}{\partial\mathbf{J}_q}. \tag{13}$$

From Eq. (10), one can obtain the nucleon effective mass m_q^* , i.e.,

$$\begin{aligned}
\frac{\hbar^2}{2m_q^*} = & \frac{\hbar^2}{2m} + (B_1 + B_4\rho^\beta + B_5\rho^\gamma)\rho \\
& - t_q(B'_1 + B'_4\rho^\beta + B'_5\rho^\gamma)\tilde{\rho}, \tag{14}
\end{aligned}$$

the single nucleon potential (without Coulomb potential)

$$\begin{aligned}
U_q = & B_0\rho - t_q B_0'\tilde{\rho} + B_1\tau - t_q B_1'\tilde{\tau} + \frac{\alpha+2}{2}B_3\rho^{\alpha+1} - \frac{B_3'}{2}(\alpha\tilde{\rho} + 2t_q\rho)\rho^{\alpha-1}\tilde{\rho} \\
& + (\beta+1)B_4\rho^\beta\tau + (\gamma+1)B_5\rho^\gamma\tau - (B_4'\beta\rho^\beta + B_5'\gamma\rho^\gamma)\tilde{\rho}\tilde{\tau} - t_q(B_1' + B_4'\rho^\beta + B_5'\rho^\gamma)\tilde{\tau} \\
& - \frac{\beta(2\beta+3)B_4\rho^{\beta-1} - B_5'\gamma\rho^{\gamma-1}}{4}(\nabla\rho)^2 - \frac{2B_2 + (2\beta+3)B_4\rho^\beta - B_5'\rho^\gamma}{2}\nabla^2\rho \\
& - \frac{3\beta B_4'\rho^{\beta-1} - \gamma B_5'\rho^{\gamma-1}}{4}\nabla\tilde{\rho} \cdot (2t_q\nabla\rho + \nabla\tilde{\rho}) - \frac{2B_2' + 3B_4'\rho^\beta - B_5'\rho^\gamma}{2}t_q\nabla^2\tilde{\rho} \\
& + \frac{\beta B_4'}{2}\rho^{\beta-1}(\nabla\tilde{\rho})^2 + \frac{\beta B_4'}{2}\rho^{\beta-1}\tilde{\rho}\nabla^2\tilde{\rho} + \frac{\beta(\beta-1)B_4'}{2}\rho^{\beta-2}\tilde{\rho}(\nabla\rho)^2t_q + \frac{\beta B_4'}{2}\rho^{\beta-1}\tilde{\rho}(\nabla^2\rho)t_q \\
& + \frac{\beta C_2\rho^{\beta-1} + \gamma C_3\rho^{\gamma-1}}{2}J^2 + \frac{\beta C_2'\rho^{\beta-1} + \gamma C_3'\rho^{\gamma-1}}{2}J^2 - \frac{b_{IS}}{2}\nabla \cdot J - t_q \frac{b_{IV}}{2}\nabla \cdot \tilde{J}, \tag{15}
\end{aligned}$$

and the SO potential

$$\begin{aligned}
W_q = & \frac{b_{IS}}{2}\nabla\rho + t_q \frac{b_{IV}}{2}\nabla(\rho_n - \rho_p) \\
& + \frac{\alpha_J + \beta_J}{2}J + t_q \frac{\alpha_J - \beta_J}{2}(J_n - J_p), \tag{16}
\end{aligned}$$

where $t_q = 1$ and -1 for $q = n$ and p , respectively. The parameters α_J and β_J in the SO potentials are defined by

$$\alpha_J = \alpha_C + \alpha_T, \quad \beta_J = \beta_C + \beta_T, \tag{17}$$

with the central-exchange parameters given by

$$\begin{aligned}
\alpha_C = & 2C_1 + 2C_2\rho^\beta + 2C_3\rho^\gamma, \\
\beta_C = & 2C_1' + 2C_2'\rho^\beta + 2C_3'\rho^\gamma. \tag{18}
\end{aligned}$$

As can be seen from Eqs. (15) and (16), the coupling constants b_{IS} and b_{IV} appear in both the central potential U_q and the spin-orbit potential W_q . In contrast, the tensor force contributes exclusively to W_q , without affecting U_q .

B. Charge and weak form factors

The normalized nuclear form factors, namely the charge form factor $F_C(q)$ and the weak charge form factor $F_W(q)$, are calculated by folding the point-nucleon form factors $F_t(q)$ and spin-orbit current form factors $F_t^{ls}(q)$ ($t = n, p$) with the corresponding intrinsic nucleon electromagnetic $G_{E/M,t}$ and weak $G_{E/M,t}^{(W)}$ form factors [39]:

$$\begin{aligned}
F_C(q) = & \frac{1}{Z} \sum_{t=p,n} \left[G_{E,t}(q)F_t(q) + G_{M,t}(q)F_t^{ls}(q) \right], \\
F_W(q) = & \sum_{t=p,n} \frac{\left[G_{E,t}^{(W)}(q)F_t(q) + G_{M,t}^{(W)}(q)F_t^{ls}(q) \right]}{ZQ_p^{(W)} + NQ_n^{(W)}}, \tag{19}
\end{aligned}$$

where $N(Z)$ is the neutron (proton) number, and $Q_p^{(W)} = 0.0713$ and $Q_n^{(W)} = -0.9888$ are proton and

neutron weak charges, respectively. The $G_{E/M,t}$ are derived from the isospin-coupled Sachs form factors, the relativistic Darwin correction has been included and the center-of-mass corrections are taken into account by simply renormalizing the nucleon mass m_N to $(1-1/A)m_N$ in the HF calculation (see, e.g., Ref. [13] for details). The weak intrinsic nucleon form factors $G_{E/M,t}^{(W)}$ are then determined by [39]

$$\begin{aligned}
G_{E/M,n}^{(W)} = & Q_n^{(W)}G_{E/M,p} + Q_p^{(W)}G_{E/M,n} + Q_n^{(W)}G_{E/M,s}, \\
G_{E/M,p}^{(W)} = & Q_p^{(W)}G_{E/M,p} + Q_n^{(W)}G_{E/M,n} + Q_n^{(W)}G_{E/M,s}, \tag{20}
\end{aligned}$$

with the strange-quark electromagnetic form factors $G_{E/M,s}$ given by

$$\begin{aligned}
G_{E,s}(q) = & \rho_s \frac{\hbar^2 q^2 / (4c^2 m_N^2)}{1 + 4.97 \hbar^2 q^2 / (4c^2 m_N^2)}, \\
G_{M,s}(q) = & \frac{\kappa_s}{\left(1 + \frac{q^2}{12\kappa_s} r_{M,s}^2\right)^2}. \tag{21}
\end{aligned}$$

Here, the strange quark electric coupling $\rho_s = -0.24$ [40, 41], the strange magnetic moment $\kappa_s = -0.017$ [42], and the strange magnetic radius $r_{M,s}^2 = -0.015 \text{ fm}^2$ [42].

III. RESULTS

A. Single-particle energy spectrum of ^{48}Ca and ^{208}Pb

According to Ref. [19], an EDF with a strong isovector spin-orbit (IVSO) interaction is shown to simultaneously reproduce the $\Delta F_{CW}(^{48}\text{Ca})$ from the CREX experiment [18] and the $\Delta F_{CW}(^{208}\text{Pb})$ from the PREX-II experiment [43] within one sigma uncertainty. This is achieved with a strong IVSO strength of $b_{IV} \approx 250$

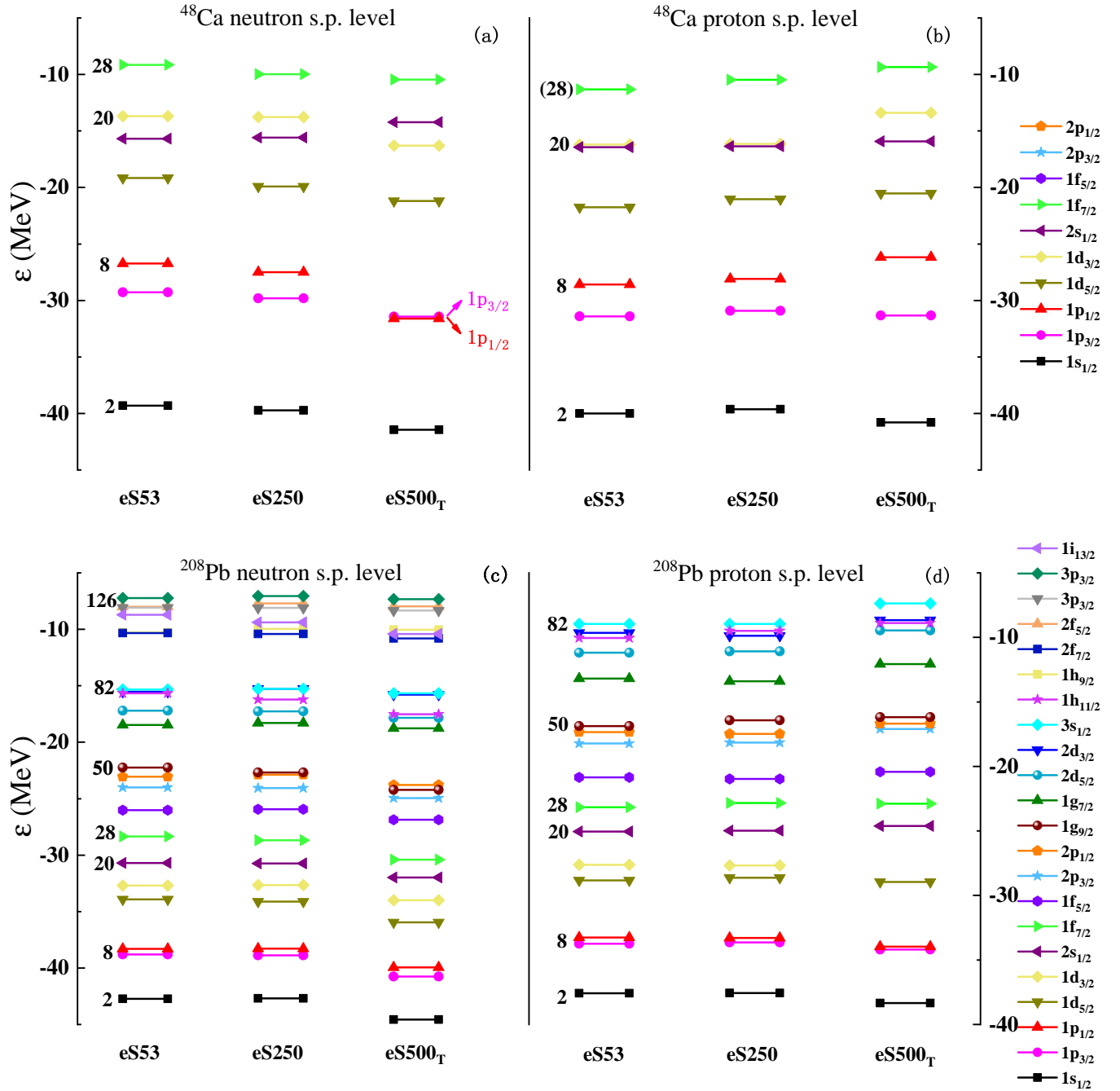


FIG. 1. Single-particle energy levels for ^{48}Ca and ^{208}Pb . Panel (a) shows neutron levels in ^{48}Ca ; panels (b)-(d) display proton levels in ^{48}Ca , neutron levels in ^{208}Pb , and proton levels in ^{208}Pb , respectively.

$\text{MeV}\cdot\text{fm}^5$, corresponding to the eS250 EDF in Ref. [19]. For this EDF, the description of ground-state nuclear properties, such as binding energies, charge radii, and spin-orbit splittings of single-particle levels, as well as selected excited-state observables including the giant monopole resonance in ^{208}Pb and the electric dipole polarizability α_D , remains in good agreement with experimental data [19]. In addition, the pure neutron matter (PNM) equation of state (EOS) predicted by this EDF

is consistent with microscopic chiral effective field theory (ChEFT) [19].

Moreover, owing to the enhanced IVSO interaction which further promotes spin-orbit splitting, the single-particle levels and shell structure of many nuclei are affected, with potential implications for magic numbers. A further examination of the single-particle spectra of ^{208}Pb and ^{48}Ca , as shown in Figure 1, reveals that eS250 reproduces the magic shell closures as well as the con-

ventional IVSO-strength EDF eS53 [19]. However, when the IVSO interaction is further enhanced using the EDF eS500_T with an extremely strong strength from Ref. [19], the single-particle energies in ⁴⁸Ca and ²⁰⁸Pb exhibit certain shifts compared to those obtained with eS53 and eS250. Nevertheless, the magic number structure remains well reproduced, although it slightly violates the usual energy level ordering of the neutron 1p_{3/2} and 1p_{1/2} states in ⁴⁸Ca. It is worth emphasizing that when b_{IV} is set to as high as 500 MeV·fm⁵ as in the eS500_T, such a extremely large IVSO strength significantly alters the spin-orbit splittings. To partially compensate for these effects, the tensor force is included in the eS500_T EDF (see Supplemental Material (SM) in Ref. [19]). Moreover, the eS500_T fails to reproduce the α_D in ²⁰⁸Pb and violates the PNM EOS from microscopic ChEFT calculations. This indicates that a b_{IV} value of 500 MeV·fm⁵ is excessively large, whereas $b_{IV} \approx 250$ MeV·fm⁵ represents a more appropriate value.

B. Sensitivity of ΔF_{CW} to the IVSO interaction for ⁴⁸Ca, ²⁰⁸Pb, ⁹⁰Zr, and ⁶²Ni

1. ⁴⁸Ca and ²⁰⁸Pb

As elucidated in Ref. [19], the sensitivity of ⁴⁸Ca to the IVSO interaction originates from the eight neutrons occupying the 1f_{7/2} orbital. This distinction between ⁴⁸Ca and ²⁰⁸Pb can be traced to the IVSO energy term $\frac{b_{IV}}{2} \tilde{J} \cdot \nabla \tilde{\rho}$ in Eq. (10). As shown in Ref. [19], in ⁴⁸Ca, all proton spin-orbit partners are filled, while the neutron 1f_{7/2} orbital is fully occupied and its 1f_{5/2} partner is empty. This configuration produces a large \tilde{J} , enabling the IVSO interaction to modify the central mean field and induce global density rearrangements that alter the contribution of every orbital to ΔF_{CW} . In ²⁰⁸Pb, by contrast, the spin-orbit unsaturated orbitals (1h_{11/2} for protons and 1i_{13/2} for neutrons) yield comparable positive contributions to J_p and J_n , resulting in a small \tilde{J} and hence a weak IVSO effect. A detailed orbital-by-orbital analysis of F_C and F_W for ⁴⁸Ca and ²⁰⁸Pb, comparing the eS53 and eS250 EDFs, can be found in the lower panel of Fig. S5 in the SM of Ref. [19]. As shown there, the contributions in ⁴⁸Ca exhibit clear differences across all orbitals when varying the IVSO interaction strength, with the most pronounced variation appearing in the 1d_{3/2} rather than 1f_{7/2} orbital—a consequence of the mean-field rearrangement induced by the IVSO interaction. In contrast, the orbital contributions in ²⁰⁸Pb remain almost unchanged, confirming its insensitivity to the IVSO interaction.

From this perspective, one can understand why a strong IVSO interaction is capable of simultaneously describing the CREX and PREX-II results. If one instead maintains the IVSO interaction at its conventional strength (i.e., $b_{IV} = b_{IS}/3$) and attempts to adjust the

tensor force strengths α_T and β_T , one finds that a simultaneous description of the CREX and PREX-II results remains unattainable, despite the fact that the tensor force and the IVSO interaction often appear similar in certain respects, such as their ability to modify the ordering of single-particle levels as noted in Ref. [19]. The key distinction between the two can be seen from Eqs. (15) and (16). The IVSO interaction contributes to both the central potential U and the spin-orbit potential W , whereas the tensor force contributes only to the spin-orbit potential W . It is precisely this modification of the central potential U by the IVSO interaction that significantly alters the contributions of all orbitals to F_C and F_W [19].

2. ⁹⁰Zr and ⁶²Ni

Following the same line of reasoning used in Ref. [19] to analyze the contribution of single-particle orbitals to the IVSO term in the energy density (Eq. (10)), one can infer that nuclei with a spin-orbit pattern analogous to ⁴⁸Ca, such as ⁹⁰Zr, should also exhibit sensitivity to the IVSO interaction in their ΔF_{CW} values. Conversely, nuclei similar to ²⁰⁸Pb, such as ⁶²Ni, are expected to be insensitive to the IVSO interaction. Applying the analysis framework of Ref. [19], one finds that in ⁹⁰Zr, the proton orbitals are spin-orbit saturated, whereas the neutron orbitals are spin-orbit unsaturated, with ten neutrons occupying the 1g_{9/2} orbital playing a role analogous to that of the eight neutrons in the 1f_{7/2} orbital of ⁴⁸Ca. In contrast, ⁶²Ni exhibits spin-orbit unsaturation in both proton and neutron channels: eight protons occupy the 1f_{7/2} orbital, and eight neutrons occupy the same orbital. Consequently, the IVSO contribution to the energy density, which is proportional to \tilde{J} , becomes nearly vanishing.

To illustrate this point, we perform an analysis for ⁹⁰Zr and ⁶²Ni analogous to that presented in the lower panel of Fig. S5 in the SM of Ref. [19] for ⁴⁸Ca and ²⁰⁸Pb. As these nuclei are open-shelled, pairing effects must be taken into account. We again compare results obtained with the eS53 and eS250 EDFs, with the proton and neutron pairing strengths determined by fitting the pairing gaps of ¹⁴⁴Sm and ¹²⁰Sn [44], respectively, using eS250. The resulting orbital-by-orbital contributions to F_C and F_W are presented in Figure 2(a)-(d). For ⁹⁰Zr, as shown in Figure 2(a) and (c), each orbital exhibits noticeable differences in its contribution when comparing eS53 and eS250. The most pronounced difference in the contribution to F_C appears in the 1d_{3/2} orbital, while for F_W , the largest difference is observed in the 1f_{5/2} orbital. For ⁶²Ni, as shown in Figure 2(b) and (d), the orbital contributions to both F_C and F_W are almost identical between eS53 and eS250, confirming our expectation. Meanwhile, we note that the differences in the orbital contributions to F_C and F_W between eS53 and eS250 are not as pronounced for ⁹⁰Zr as they are for ⁴⁸Ca, nor are they as negligible for ⁶²Ni as they are for ²⁰⁸Pb. This behavior

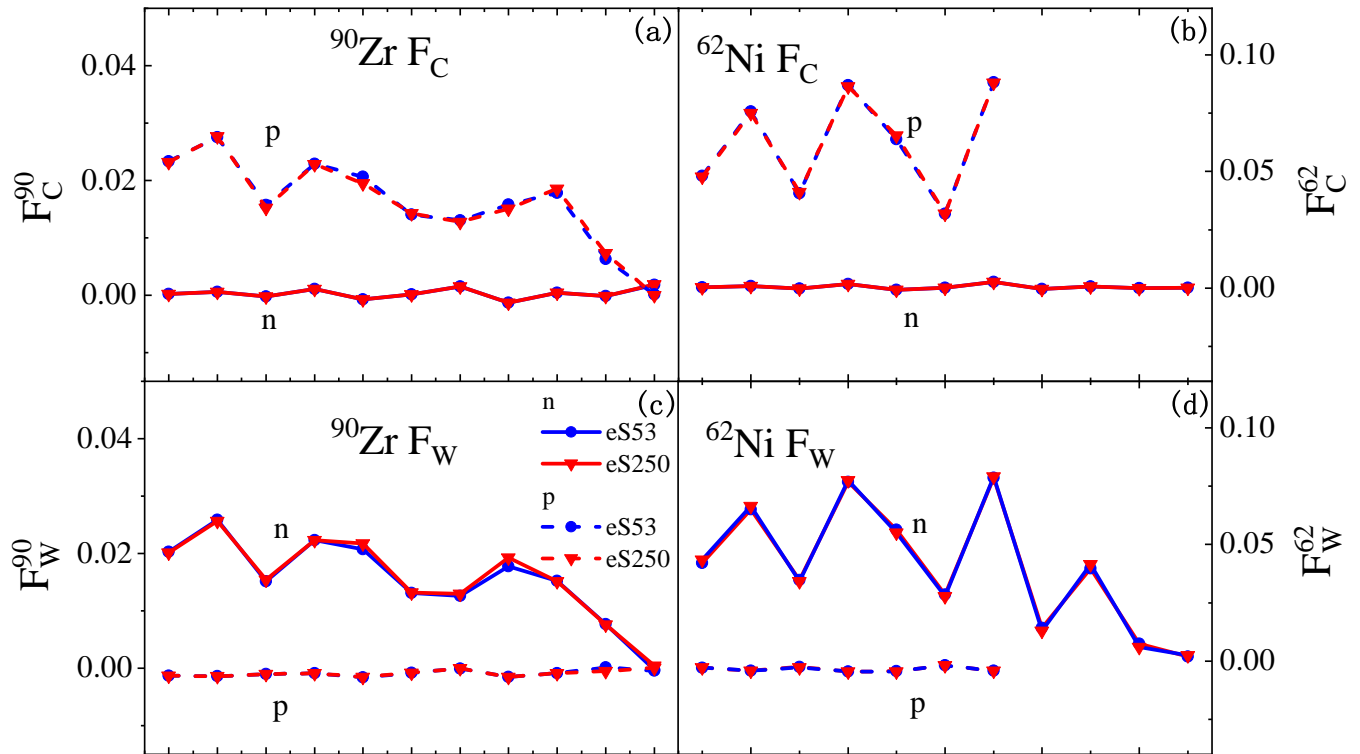


FIG. 2. Orbital contributions to F_C and F_W obtained with the eS53 and eS250 EDFs. Panels (a) and (c) show the contributions to F_C and F_W for ^{90}Zr , respectively. Panels (b) and (d) show the corresponding results for ^{62}Ni . The analyzed orbitals (from left to right) include $1s_{1/2}$, $1p_{3/2}$, $1p_{1/2}$, $1d_{5/2}$, $1d_{3/2}$, $2s_{1/2}$, $1f_{7/2}$, $1f_{5/2}$, $2p_{3/2}$, $2p_{1/2}$, and $1g_{9/2}$, both for ^{90}Zr and ^{62}Ni .

can be attributed, on the one hand, to the diminished influence of the IVSO interaction in heavier nuclei relative to lighter ones, and on the other hand, to the increased number of orbitals contributing in heavier nuclear systems.

A complementary perspective on this sensitivity is provided by the momentum-transfer dependence of ΔF_{CW} . Figure 3 displays this quantity for ^{90}Zr and ^{62}Ni in panels (c) and (d), respectively, with panels (a) and (b) showing the corresponding results for ^{48}Ca and ^{208}Pb for comparison. The comparison reveals that both ^{48}Ca and ^{90}Zr exhibit sensitivity to the IVSO interaction. For ^{90}Zr , this sensitivity is most pronounced at $q \approx 0.68 \text{ fm}^{-1}$. In contrast, ^{62}Ni and ^{208}Pb are both insensitive to the IVSO interaction.

The contrasting behavior between the pairs (^{48}Ca , ^{90}Zr) and (^{208}Pb , ^{62}Ni) makes comprehensive experimental measurements on these nuclei particularly meaningful and important. ^{90}Zr is a stable natural isotope of zirconium with an abundance of 51.45% in nature [45], while ^{62}Ni is likewise a stable natural isotope of nickel with an abundance of 3.63% [45]. Both are suitable for experimental measurements. Owing to the insensitivity of ^{208}Pb and ^{62}Ni to the IVSO interaction, parity-violating electron scattering (PVES) experiments measuring ΔF_{CW} (or the neutron skin thickness) on these two nuclei would provide a combined constraint on the symmetry energy that is more precise than that obtained

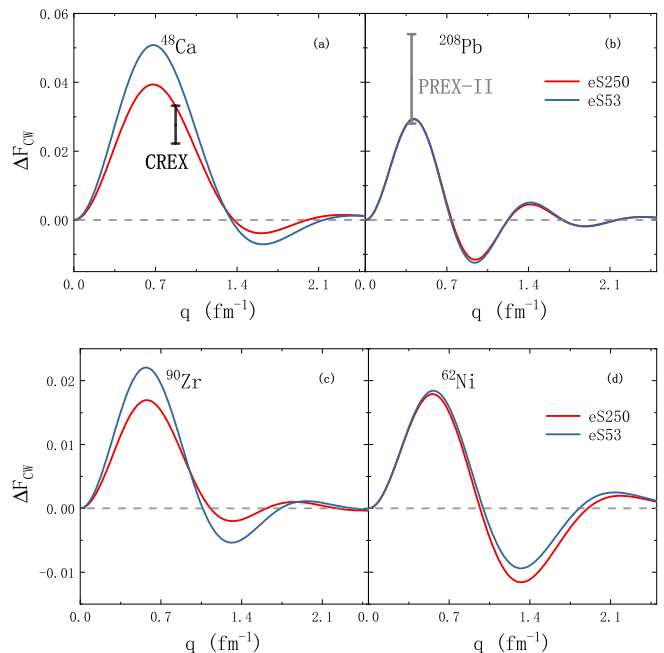


FIG. 3. Momentum-transfer dependence of ΔF_{CW} for various nuclei. Panels (a)-(d) show the results for ^{48}Ca , ^{208}Pb , ^{90}Zr , and ^{62}Ni , respectively, as functions of the momentum transfer q (in fm^{-1}). For comparison, the CREX and PREX-II data [18] (with one sigma uncertainty) are also included in panels (a) and (b), respectively.

from PREX-II alone. Meanwhile, PVES measurements on ^{90}Zr , when combined with the CREX results, would enable a more accurate determination of the IVSO interaction strength b_{IV} . Such measurements can be realistically performed at existing and upcoming facilities. The MESA accelerator in Mainz, with its planned PVES program MREX [46], is well suited for precision measurements on nuclei including ^{90}Zr and ^{62}Ni as well as ^{48}Ca and ^{208}Pb . Complementary measurements JLab, building on the successful PREX-II and CREX experiments, are also feasible as demonstrated by recent proposals and feasibility studies [47, 48]. This would have a positive and significant impact on deepening our understanding of both the symmetry energy and the IVSO interaction.

C. Neutron skin R_{np} of ^{48}Ca , ^{208}Pb , ^{90}Zr , ^{62}Ni , ^{22}O and ^{24}O

Compared to ΔF_{CW} , the neutron skin thickness R_{np} is a more intuitive and frequently discussed quantity, which, like ΔF_{CW} , characterizes the overall difference between neutron and proton distributions. Beyond ^{48}Ca and ^{90}Zr , following the analysis in Ref. [19], one can readily identify ^{22}O and ^{24}O as nuclei that are also sensitive to the IVSO interaction, with evidence supporting their double magic nature [49, 50]. Table I presents the calculated R_{np} values for ^{48}Ca , ^{208}Pb , ^{90}Zr , ^{62}Ni , ^{22}O , and ^{24}O obtained with the eS53 and eS250 EDFs. For ^{208}Pb and ^{62}Ni , the results from the two EDFs are nearly identical. In contrast, for ^{48}Ca , ^{90}Zr , ^{22}O , and ^{24}O , the eS250 predictions are smaller than those of eS53, reflecting a behavior similar to that observed for ΔF_{CW} . It is worth noting that the charge-exchange reaction measurement by Ref. [51] reported $\Delta R_{\text{np}} = 0.07 \pm 0.04$ fm for ^{90}Zr , with the central value of 0.07 fm lying between the eS250 and eS53 predictions, indicating the need for more precise experimental determinations. Furthermore, future measurements of R_{np} for ^{22}O and ^{24}O , e.g., by charge-changing cross sections [52, 53], would be highly desirable to validate the predictions of the present work.

TABLE I. Neutron skin R_{np} (in fm) of ^{48}Ca , ^{208}Pb , ^{90}Zr , ^{62}Ni , ^{22}O and ^{24}O with eS53 and eS250.

Nucleus	eS53	eS250
^{48}Ca	0.179	0.129
^{208}Pb	0.199	0.195
^{90}Zr	0.083	0.053
^{62}Ni	0.096	0.093
^{22}O	0.367	0.290
^{24}O	0.510	0.430

IV. CONCLUSIONS

In this work, we have systematically investigated the sensitivity of the charge-weak form factor difference ΔF_{CW} to the IVSO interaction of ^{48}Ca , ^{208}Pb , ^{90}Zr and ^{62}Ni , using the extended Skyrme EDFs eS53 and eS250. Our analysis reveals that a strong IVSO interaction, with $b_{\text{IV}} \approx 250$ MeV·fm⁵, not only resolves the PREX-CREX puzzle but also preserves the established magic shell closures in ^{48}Ca and ^{208}Pb , as well as gives good description of nuclear global properties.

By examining the orbital-by-orbital contributions to F_{C} and F_{W} , we demonstrate that the sensitivity of ^{48}Ca originates from the eight $1f_{7/2}$ neutrons, which modify the central mean-field potential and thereby influence all orbitals. A similar mechanism is identified in ^{90}Zr , where ten $1g_{9/2}$ neutrons play an analogous role, leading to a pronounced IVSO sensitivity in its ΔF_{CW} and neutron skin thickness R_{np} . In contrast, ^{208}Pb and ^{62}Ni , characterized by near-cancellation of the isovector spin-orbit density $J_{\text{n}} - J_{\text{p}}$, exhibit little sensitivity to the IVSO interaction.

This structural distinction between the pairs (^{48}Ca , ^{90}Zr) and (^{208}Pb , ^{62}Ni) offers a powerful strategy for disentangling the IVSO interaction from the density dependence of the symmetry energy. The natural abundances and experimental accessibility of ^{90}Zr and ^{62}Ni make them ideal candidates for future PVES measurements. Combined with existing PREX-II and CREX data, such experiments could be performed in MREX and JLab, which would enable a more precise determination of both the symmetry energy slope L and the IVSO strength b_{IV} .

Furthermore, our predictions for the neutron skin thickness in ^{22}O and ^{24}O , which could be measured by charge-changing cross sections, suggest that these neutron-rich oxygen isotopes are also sensitive to the IVSO interaction, offering additional testing grounds for the proposed strong IVSO scenario. The present findings underscore the importance of nucleus-dependent observables in constraining poorly known isovector components of the nuclear force, and highlight the potential of PVES experiments to provide new insights into the nucleus-dependent spin-orbit saturation that governs the sensitivity to the IVSO interaction.

ACKNOWLEDGEMENTS.

This work was supported in part by the National Natural Science Foundation of China under Grant Nos. 12235010, 11905302 and 11625521, the National SKA Program of China No. 2020SKA0120300, and the Science and Technology Commission of Shanghai Municipality under Grant No. 23JC1402700.

- [1] L. H. Thomas, The motion of a spinning electron, *Nature* **117**, 514 (1926).
- [2] P. A. M. Dirac, The quantum theory of the electron, *Proc. Roy. Soc. Lond. A* **117**, 610 (1928).
- [3] Z.-T. Liang and X.-N. Wang, Globally polarized quark-gluon plasma in non-central A+A collisions, *Phys. Rev. Lett.* **94**, 102301 (2005), [Erratum: *Phys. Rev. Lett.* **96**, 039901 (2006)].
- [4] L. Adamczyk *et al.* (STAR), Global Λ hyperon polarization in nuclear collisions: evidence for the most vortical fluid, *Nature* **548**, 62 (2017).
- [5] G. Bihlmayer, P. Noel, D. V. Vyalikh, E. V. Chulkov, and A. Manchon, Rashba-like physics in condensed matter, *Nature Rev. Phys.* **4**, 642– (2022).
- [6] K. Y. Bliokh, F. J. Rodríguez-Fortuño, F. Nori, and A. V. Zayats, Spin-orbit interactions of light, *Nature Photon.* **9**, 796 (2015).
- [7] S. A. Goudschmidt and G. H. Uhlenbeck, Spinning electrons and the structure of spectra, *Nature* **117**, 264 (1926).
- [8] M. G. Mayer, On closed shells in nuclei. 2, *Phys. Rev.* **75**, 1969 (1949).
- [9] O. Haxel, J. H. D. Jensen, and H. E. Suess, On the "Magic Numbers" in Nuclear Structure, *Phys. Rev.* **75**, 1766 (1949).
- [10] V. I. Isakov, K. I. Erokhina, H. Mach, M. Sanchez-Vega, and B. Fogelberg, On the difference between proton and neutron spin orbit splittings in nuclei, *Eur. Phys. J. A* **14**, 29 (2002).
- [11] T. Lesinski, M. Bender, K. Bennaceur, T. Duguet, and J. Meyer, The Tensor part of the Skyrme energy density functional. I. Spherical nuclei, *Phys. Rev. C* **76**, 014312 (2007).
- [12] P. Klupfel, P. G. Reinhard, T. J. Burvenich, and J. A. Maruhn, Variations on a theme by Skyrme: A systematic study of adjustments of model parameters, *Phys. Rev. C* **79**, 034310 (2009).
- [13] M. Bender, P.-H. Heenen, and P.-G. Reinhard, Self-consistent mean-field models for nuclear structure, *Rev. Mod. Phys.* **75**, 121 (2003).
- [14] M. M. Sharma, G. Lalazissis, J. König, and P. Ring, Isospin Dependence of the Spin-Orbit Force and Effective Nuclear Potentials, *Phys. Rev. Lett.* **74**, 3744 (1995).
- [15] P.-G. Reinhard and H. Flocard, Nuclear effective forces and isotope shifts, *Nuclear Physics A* **584**, 467488 (1995).
- [16] J. P. Ebran, A. Mutschler, E. Khan, and D. Vretenar, Spin-orbit interaction in relativistic nuclear structure models, *Phys. Rev. C* **94**, 024304 (2016).
- [17] D. Vautherin and D. M. Brink, Hartree-Fock calculations with Skyrme's interaction. 1. Spherical nuclei, *Phys. Rev. C* **5**, 626 (1972).
- [18] D. Adhikari *et al.* (CREX), Precision Determination of the Neutral Weak Form Factor of Ca48, *Phys. Rev. Lett.* **129**, 042501 (2022).
- [19] T.-G. Yue, Z. Zhang, and L.-W. Chen, Evidence for strong isovector nuclear spin-orbit interaction, *Sci. Bull.* [10.1016/j.scib.2026.01.062](https://doi.org/10.1016/j.scib.2026.01.062) (2024).
- [20] P.-G. Reinhard, X. Roca-Maza, and W. Nazarewicz, Combined Theoretical Analysis of the Parity-Violating Asymmetry for Ca48 and Pb208, *Phys. Rev. Lett.* **129**, 232501 (2022).
- [21] E. Yüksel and N. Paar, Implications of parity-violating electron scattering experiments on 48Ca (CREX) and 208Pb (PREX-II) for nuclear energy density functionals, *Phys. Lett. B* **836**, 137622 (2023).
- [22] Z. Zhang and L.-W. Chen, Bayesian inference of the symmetry energy and the neutron skin in Ca48 and Pb208 from CREX and PREX-2, *Phys. Rev. C* **108**, 024317 (2023).
- [23] C. Mondal and F. Gulminelli, Nucleonic metamodelling in light of multimessenger, PREX-II, and CREX data, *Phys. Rev. C* **107**, 015801 (2023).
- [24] S. Tagami, T. Wakasa, and M. Yahiro, Slope parameters determined from CREX and PREX2 (published in Results in Physics) [10.48550/arXiv.2210.03313](https://arxiv.org/abs/10.48550/arXiv.2210.03313) (2022).
- [25] T. Miyatsu, M.-K. Cheoun, K. Kim, and K. Saito, Can the PREX-2 and CREX results be understood by relativistic mean-field models with the astrophysical constraints?, *Phys. Lett. B* **843**, 138013 (2023).
- [26] F. Sammarruca, The Neutron Skin of ^{48}Ca and ^{208}Pb : A Critical Analysis, *Symmetry* **16**, 34 (2024).
- [27] P. Papakonstantinou, Nuclear symmetry energy and the PREX-CREX neutron skin puzzle within the KIDS framework (2022) [arXiv:2210.02696 \[nucl-th\]](https://arxiv.org/abs/2210.02696).
- [28] M. Kumar, S. Kumar, V. Thakur, R. Kumar, B. K. Agrawal, and S. K. Dhiman, CREX- and PREX-II-motivated relativistic interactions and their implications for the bulk properties of nuclear matter and neutron stars, *Phys. Rev. C* **107**, 055801 (2023).
- [29] J. M. Lattimer, Constraints on Nuclear Symmetry Energy Parameters, *Particles* **6**, 30 (2023).
- [30] N. Liliani, A. M. Nugraha, J. P. Dinningrum, and A. Sulaksono, Tensor and isovector-isoscalar terms of relativistic mean field model: Impacts on neutron-skin thickness, charge radius, and nuclear matter, *Nucl. Phys. A* **1042**, 122812 (2024).
- [31] A. Kunjipurayil, J. Piekarewicz, and M. Salinas, Role of the isovector spin-orbit potential in mitigating the CREX-PREX dilemma, *Phys. Rev. C* **112**, 014310 (2025).
- [32] T. Zhao, Z. Lin, B. Kumar, A. W. Steiner, and M. Prakash, Characterizing the nuclear models informed by PREX and CREX: A view from Bayesian inference, *Phys. Rev. Res.* **7**, 043335 (2025).
- [33] M. Qiu, T.-G. Yue, Z. Zhang, and L.-W. Chen, Resolving the PREX-CREX puzzle in covariant density functional theory, (2025).
- [34] N. Chamel, S. Goriely, and J. M. Pearson, Further explorations of Skyrme-Hartree-Fock-Bogoliubov mass formulas. XI. Stabilizing neutron stars against a ferromagnetic collapse, *Phys. Rev. C* **80**, 065804 (2009).
- [35] F. Stancu, D. M. Brink, and H. Flocard, The tensor part of Skyrme's interaction, *Phys. Lett. B* **68**, 108 (1977).
- [36] E. Chabanat, J. Meyer, P. Bonche, R. Schaeffer, and P. Haensel, A Skyrme parametrization from subnuclear to neutron star densities, *Nucl. Phys. A* **627**, 710 (1997).
- [37] Z. Zhang and L.-W. Chen, Extended Skyrme interactions for nuclear matter, finite nuclei and neutron stars, *Phys. Rev. C* **94**, 064326 (2016).
- [38] M. V. Stoitsov, J. Dobaczewski, W. Nazarewicz, and P. Ring, Axially deformed solution of the Skyrme-Hartree-Fock-Bogolyubov equations using the trans-

- formed harmonic oscillator basis: The Program HF-BTHO (v1.66p), *Comput. Phys. Commun.* **167**, 43 (2005).
- [39] P.-G. Reinhard, X. Roca-Maza, and W. Nazarewicz, Information Content of the Parity-Violating Asymmetry in Pb208, *Phys. Rev. Lett.* **127**, 232501 (2021).
- [40] A. Acha *et al.* (HAPPEX), Precision Measurements of the Nucleon Strange Form Factors at $Q^{*2} \sim 0.1\text{-GeV}^{*2}$, *Phys. Rev. Lett.* **98**, 032301 (2007).
- [41] J. Liu, R. D. McKeown, and M. J. Ramsey-Musolf, Global Analysis of Nucleon Strange Form Factors at Low Q^{*2} , *Phys. Rev. C* **76**, 025202 (2007).
- [42] C. Alexandrou, S. Bacchio, M. Constantinou, J. Finkenrath, K. Hadjiyiannakou, K. Jansen, and G. Koutsou, Nucleon strange electromagnetic form factors, *Phys. Rev. D* **101**, 031501 (2020).
- [43] D. Adhikari *et al.* (PREX), Accurate Determination of the Neutron Skin Thickness of ^{208}Pb through Parity-Violation in Electron Scattering, *Phys. Rev. Lett.* **126**, 172502 (2021).
- [44] M. Bender, K. Rutz, P. G. Reinhard, and J. A. Maruhn, Pairing gaps from nuclear mean field models, *Eur. Phys. J. A* **8**, 59 (2000).
- [45] National Nuclear Data Center, information extracted from the NuDat database, <https://www.nndc.bnl.gov/nudat/>.
- [46] S. Schlimme *et al.*, The MESA physics program, *EPJ Web Conf.* **303**, 06002 (2024).
- [47] A. Esser *et al.*, Beam-Normal Single-Spin Asymmetry in Pb208 at Low Energy: Discrepancy Resolved or New Kinematic Puzzle?, *Phys. Rev. Lett.* **135**, 232502 (2025).
- [48] C. Gal *et al.*, Nuclear Dependence of Beam Normal Single Spin Asymmetry in Elastic Scattering from Nuclei, (2024).
- [49] A. Ozawa, T. Kobayashi, K. Suzuki, K. Yoshida, and I. Tanihata, A new magic number, $N=16$, Near to the neutron drip-line, *Phys. Rev. Lett.* **84**, 5493 (2000).
- [50] E. Becheva *et al.*, $N=14$ Shell Closure in O-22 Viewed through a Neutron Sensitive Probe, *Phys. Rev. Lett.* **96**, 012501 (2006).
- [51] K. Yako, H. Sagawa, and H. Sakai, Neutron skin thickness of Zr-90 determined by charge exchange reactions, *Phys. Rev. C* **74**, 051303 (2006).
- [52] J. Zhang *et al.* (Super-FRS), A new approach for deducing rms proton radii from charge-changing reactions of neutron-rich nuclei and the reaction-target dependence, *Sci. Bull.* **69**, 1647 (2024).
- [53] Z. Hasan, M. Imran, A. A. Usmani, and Z. A. Khan, Theoretical investigation of charge-changing cross section and interaction cross section for Be, B, C, N, O, and F isotopes on C12 at 200–1050 MeV/nucleon, *Phys. Rev. C* **111**, 064601 (2025).